Journal of Energy Storage 115 (2025) 115911

Contents lists available at ScienceDirect

Journal of Energy Storage

journal homepage: www.elsevier.com/locate/est

Research papers

Influence of current tabs on performance and aging of multi-tab 26650-type LFP lithium-ion batteries

D. Petz [a,b], M.J. Mühlbauer [b,c], V. Baran [b,d], J. Rebelo Kornmeier [b], A. Schökel [d], T. Pirling [e], P. Müller-Buschbaum [a], A. Senyshyn [b,*]

[a] Department of Physics, Chair for Functional Materials, TUM School of Natural Sciences, Technical University of Munich, James-Franck-Str. 1, 85748 Garching, Germany
[b] Heinz Maier-Leibnitz Zentrum (MLZ), Technical University of Munich, Lichtenbergstraße 1, 85748 Garching, Germany
[c] Institute for Applied Materials (IAM), Karlsruhe Institute of Technology (KIT), Hermann-von-Helmholtz-Platz 1, 76344 Eggenstein-Leopoldshafen, Germany
[d] Deutsches Elektronen Synchrotron DESY, Notkestr. 85, 22607 Hamburg, Germany
[e] Institute Max von Laue – Paul Langevin (ILL), 71, Avenue des Martyrs, 38043 Grenoble Cedex 9, France

ARTICLE INFO

Keywords:
Lithium distribution
X-ray diffraction computed tomography
Neutron powder diffraction
Cell geometry

ABSTRACT

Two high-power lithium-ion batteries of 26650-type adopting $LiFePO_4$|C cell chemistry are non-invasively characterized using electrochemical, thermodynamical, and diffraction-based methods. Their discharging and charging behavior are probed using incremental capacity analysis and differential voltage analysis normalized to the state-of-charge. Differential thermal analysis allows for a qualitative probe of the electrolyte subsystem in both cells. Diffraction-based non-destructive characterization using both synchrotron and neutron radiation (in the form of X-ray diffraction computed tomography and spatially-resolved neutron diffraction) reveals the state-of-lithiation for cathode and anode materials in the fully-charged state at *operando* conditions. Electrochemical characteristics, influence of cell geometry, and state-of-lithiation are compared and discussed, and their effect and interplay are elucidated in detail.

1. Introduction

Rapid growth of electromobility put new focuses on the development of lithium-ion batteries, where the most important aspect is safety. Among the commonly used cathode materials such as lithium cobalt oxide (LCO), lithium nickel manganese cobalt oxide (NMC), lithium nickel aluminum cobalt oxide (NCA) and lithium iron phosphate (LFP), the latter provides the safest chemistry [1], leading to an increasing share of LFP batteries in the global battery market. Besides this, LFP possesses extraordinary cycling rate capabilities, which enable high peak currents, thus making them suitable for high-power applications, i.e., for fast acceleration and kinetic energy recovery during deceleration. Unfortunately, the theoretical achievable gravimetric energy density of LFP (170 mAh/g) cells is below those of LCO (274 mAh/g), NMC (275 mAh/g) and NCA (279 mAh/g). Additionally, the operating voltage window of typically 2.0–3.6 V for LFP cells is lower than the voltage limits of 2.5–4.2 V for LCO/NCA/NMC. The choice of the cathode material often defines the battery type and operation mode, e.g. LCO based cathodes are frequently used in stretchable battery designs [2]. In contrast, LFP has been used for solid-state lithium metal batteries [3]. There is a steady trend towards increasing cell volume to reach higher energy and power density in new cells by minimizing the ratio between active and inactive cell material. This trend is reflected in the evolution of cylinder-type cell standards in automotive applications from 18650-type through 21700 and 26650-type batteries to 4680-type.

It has been shown for a series of 18650-type lithium-ion batteries, that non-uniform distributions of cell characteristics such as current density [4–6], and temperature [7,8] lead to an inhomogeneous usage of the electrode materials [9,10] and, therefore, to unevenly distributed lithium intercalation into the electrode materials [11–13]. The current distribution (mediated by the current tab configuration) has been shown to negatively affect the homogeneity of the electrode lithiation [11]. Spatially resolved diffraction methods are a powerful tool to investigate these inhomogeneous lithium distributions [14–18]. Since larger format cells potentially realize complex current and temperature distributions [4,19,20], the geometry of the electrical cell layout influences cell uniformity but has not yet been investigated.

The current study aims to non-destructively characterize and

* Corresponding author.
E-mail address: anatoliy.senyshyn@gmail.com (A. Senyshyn).

https://doi.org/10.1016/j.est.2025.115911
Received 28 July 2024; Received in revised form 7 January 2025; Accepted 17 February 2025
Available online 27 February 2025

compare two commercially available 26650-type lithium-ion batteries with different current tab configurations and to determine the uniformity of their properties during real cell operation. Therefore, two fresh cells are characterized using the capacity-voltage profile during dis-/charging at low current rates. Incremental capacity (dQ/dV) and differential voltage analysis (dV/dQ) are applied to characterize the lithium-ion cells in terms of aging [21–24] and heterogeneity of electrode phase transitions [25,26]. In addition to these studies, the electrolyte subsystem is probed using differential thermal analysis (DTA), which enables to qualitatively determine compositional changes of electrolytes upon cell aging [13,27,28] and tortuosity of electrodes in lithium-ion cells [29].

Finally, the assumed heterogeneous states of both cells are investigated in a fully-charged state using X-Ray diffraction computed tomography (XRD-CT) to determine the lithium-content intercalated in anode and cathode simultaneously. Since one of the cells shows strong absorption of the synchrotron radiation, measurements are completed using spatially-resolved neutron powder diffraction. Finally, an entirely non-destructive characterization of the uniformity of large format 26650-type lithium-ion batteries is reported.

2. Experimental methods

2.1. Galvanostatic cell preparation

Two commercial lithium-ion batteries (cell 1 - ANR26650M1B from A123 systems, cell 2 - K226650P01 from Emmerich) were cycled using a Neware BTS4000 multichannel potentiostat for cell characterization. The cells were discharged using a small constant current of 400 mA (corresponding to approx. C/6) to the lower potential limit of 2.0 V. Charging was carried out using a constant current of 400 mA to the upper voltage limit of 3.6 V followed by a constant voltage charging at 3.6 V with a current cut-off of 20 mA. Between dis-/charging an open circuit voltage phase was applied for 30 min to achieve cell relaxation between the individual dis-/charge cycles. Charging curves were evaluated to characterize the electrochemical behavior of both cells using incremental capacity analysis (ICA) and differential voltage analysis (DVA). In order to compensate for the different capacities of the cells, the capacity was normalized to represent the state-of-charge (SOC) of the cells.

2.2. X-ray computed tomography (CT)

Details of the cell layout (internal cell geometry and morphology) were studied using X-ray computed tomography with a phoenix v|tome|x s 240 tomography scanner. An integrated direct tube with an acceleration voltage of 130 kV and current of 100 µA was used for X-ray generation. Data was collected using a 2D high-resolution amorphous silicon detector (200 × 200 mm^2; 1000 × 1000 px) in cone-beam geometry. Using a multiscan approach implemented in the CT measurement system, the cell bottom, center and top were measured separately with little overlap to achieve improved magnification to an effective voxel linear size of $\sim 39\,\mu m$. In total, 1001 projections over the full angular range of 360° were collected, where every projection was the average of 3 single exposures of 2000 ms duration. Reconstruction was performed using phoenix datos|x software for the initial state and X-AID software for the cells after cycling. The reconstructed slices of the individual heights were merged using ImageJ [30]. VGStudio Max and ParaView [31] were used for the final visualization, including color coding of the different cell materials.

2.3. Spatially-resolved neutron powder diffraction

Spatially-resolved neutron powder diffraction was performed at the engineering diffractometer SALSA (Institut Laue-Langevin, Grenoble, France) [32]. The experimental procedure followed the previously described experiment [11]. The monochromatic neutron beam with a wavelength of $\lambda = 1.66$ Å obtained from the (400) reflection of the Si monochromator was shaped to a cross-section of 2 mm in width and 10 mm in height in front of the sample using instrumental optics. Data collection was performed at mid-height perpendicular to the cylinder axis. The gauge volume was defined by the incident neutron beam together with a radial oscillating collimator with a 1 mm horizontal field-of-view in front of the detector, which defined the horizontal cross-section. In addition to in-plane characterization, comprised of differently oriented gauge volumes, a single gauge volume was selected and scanned at various heights. A 2D position-sensitive microstrip detector with an active detector area of 80 × 80 mm^2 (256 × 256 channels) at a sample-to-detector distance of ca. 610 mm and a central scattering angle of 26 deg. covering the angular range of $\sim 24 - 31.5$ deg. The exposure time was in the range of minutes; however, for each gauge volume, the exposure was adjusted depending on the position relative to the center of the jellyroll. The 2D diffraction images were integrated into a conventional 1D diffraction pattern and evaluated by the approach described in [33].

2.4. X-ray diffraction computed tomography (XRD-CT)

X-ray diffraction computed tomography was performed at beamline P02.1 of PETRA III synchrotron (DESY, Hamburg, Germany) [34]. The incident synchrotron beam with a fixed photon energy of ~60 keV corresponding to a wavelength of $\lambda = 0.20714$ Å was shaped to a cross-section of 1 × 1 mm^2. 2D diffraction signal was acquired using a Perkin Elmer XRD1621 CN3 - EHS detector[1] located at 1976.5 mm sample-to-detector distance. The detector was positioned so that 90 degrees of the Debey-Scherrer rings were covered by the detector area, i.e. the direct beam illuminated the lower right corner. Therefore, the measured scattering angle range could be enlarged. A diffractogram was obtained by the summation of 10 single exposures, where each exposure had a length of 1 s. In between the perpendicular scans, a dark image was acquired. The scanning procedure was similar to the one reported in [35]. The obtained set of diffractograms comprised 31 translation steps perpendicular to the beam direction/axes over a width of [−15.5:15.5] mm and 31 rotations steps covering [0:180] deg. Data collection was performed at the mid-height of both cells and at the top/bottom of cell 1. The obtained set of 2D diffraction images was integrated into 1D diffraction patterns using PyFai software [36]. Finally, the integrated diffraction patterns were used as input for the reconstruction using the filtered back projection algorithm embedded in TomoPy [37].

Intensities of the 200 $LiFePO_4$ and the 200 $FePO_4$ reflections were analyzed to calculate the lithium content y in Li_yFePO_4 of the cathode, and the 001 LiC_6 and 002 LiC_{12} peaks were used to estimate the lithium content x in Li_xC_6 of the graphite anode. An example of diffraction data is presented in Fig. S1, and a detailed description of the calculation is given in the supplementary information.

2.5. Differential thermal analysis (DTA)

Differential thermal analysis characterization was performed according to the methodology reported in Ref. [13]. Measurements were performed utilizing a closed-cycle refrigerator using the temperature controller LakeShore 340. Cernox and platinum temperature sensors were used to control the temperature of the cryostat and the sample. Temperature regulation was achieved via the PID scheme, and He 4.6 was used as a heat transmitter.

The cylindrical 26650-type lithium-ion batteries and a copper cylinder reference (height: 5.8 cm; diameter: 0.8 cm; weight: 26.09 g) sample were cooled and heated within the temperature range of 100 K to 310 K at a constant temperature ramp of ∓0.5 K/min. A pair of PT1000

[1] 2048 × 2048 pixel á 200 × 200 µm^2.

temperature sensors were attached to the metallic surface of the cell, and a copper reference was used to record the temperature throughout the temperature ramp of the cryostat. Finally, the reference temperature was subtracted from the sample temperature to obtain a differential signal, reflecting the first-order phase transitions of the liquid electrolyte of the studied batteries. Although the DTA signal is independent of the SOC, measurements were usually performed in the fully-charged state.

2.6. Electrochemical cycling

The two LFP cells were cycled at room temperature with the same normalized conditions using a Neware BTS4000 potentiostat. The cells were cycled in the full voltage window of 2.0 V–3.6 V using a discharge current rate (C-rate) of 7.5C (cell 1: 18.75 A; cell 2: 19.5 A) and a charging C-rate of 1C (cell 1: 2.5 A; cell 2: 2.6 A) with an additional constant voltage phase at 3.6 V with a cut-off C-rate of 1/50C. C-rate was chosen as a tradeoff between available current of the potentiostat (20 A) and the capacity of the cells (2.5 Ah for cell 1 and 2.6 Ah for cell 2), which calculates as 20 A/2.6 Ah ≈ 7.5C. The absolute currents lie quite below the maximal allowed currents of the cells of 50 A for cell 1 and 42 A for cell 2. For cell 1, a fast charging was given with 10 A to 80 % SOC. As SOC is state-of-health dependent and was intended to change drastically, the authors decided to stay on the safe side with the recommended C-rate of 1C. After every 50th cycle, a characterization cycle was applied using a lower C-rate of 1/5C for discharging and charging. These characterization cycles were then again used for ICA and DVA evaluation. Cycling duration was defined via the typical degradation stages given in ref. [38], i.e., cells were cycled until they went through the acceleration and stabilization stage and reached the saturation stage. This procedure ensured an advanced aging state of both cell by simultaneous good comparability of the cells.

2.7. Optical measurement of cell deformation

A Keyence TM-X5065 optical micrometer was used to measure the external expansion of the investigated lithium-ion batteries. Cells were glued on top of an aluminum pin giving access to the cell surface. The cell was centered with respect to the field-of-view of the optical micrometer on top of a goniometer head and a rotation stage. Cell rotation and triggering of image capture were controlled via NICOS software [39]. The cell expansion was measured by taking 1000 images over 360° rotation and determining the cell edges by fitting a Boltzmann edge function to each side of the cell. Final visualizations were performed using ParaView [31,40] and ImageJ [41] software packages. Results of the optical measurements given in this work are stated as radii, i.e. the distance of the surface point to the rotation symmetry axis of the cell.

3. Results & discussion

The design of cylinder-type cell 1 and cell 2 is based on the electrode rollover. Their larger diameter, along with the relatively thin electrodes, would imply increasing cell heterogeneity when compared to high-energy 18650-type cells. To verify this assumption, the cell uniformity of both cell types was non-destructively studied using a combination of several complementary approaches.

3.1. General characterization (dSoC/dV; dV/dSoC; DTA; cell geometry)

3.1.1. Incremental capacity analysis

Electrochemical cell characteristics were obtained from galvanostatic characterization. Obtained cell capacities (2480.5 mAh for cell 1 and 2347.1 mAh for cell 2) agree with typical values in 18650-type cells adopting LFP|C cell chemistry.[2] Obtained capacity values were used to determine state-of-charge (SoC) 100 %. The normalized charging profile (cell potential V vs. SoC) is plotted in Fig. 1b for cells 1 and 2. Details of the charging profile resemble the typical LFP|C cell behavior, showing a series of characteristic voltage plateaus. Qualitatively similar charging profiles for cell 1 and cell 2 were observed; however, the profile for cell 2 is shifted systematically towards higher potentials and/or lower SoC compared to cell 1. Since the applied current rates were identical, the observed shift towards higher potentials can be attributed to a higher internal cell resistance [42]. An estimation of the internal resistances for both cells (using the direct current resistance $R = \Delta U/\Delta I$, where ΔU corresponds to the voltage increase 10 s after the beginning of charging and ΔI to the charging current) yields $R_{i,1} = 54.5(2)$ mΩ and $R_{i,2} = 137.7(2)$ mΩ for cell 1 and cell 2, respectively.

Differential analysis of the normalized charging profile yields dSoC/dV (corresponding to incremental capacity analysis - ICA) and dV/dSoC curves plotted in Fig. 1a and c. The differential SoC plot is represented by three characteristic plateaus marked as ①, ②, and ③, which can be directly associated with the intercalation in LFP|C cell chemistry. Since the LFP-cathode undergoes only one phase transition from the lithiated lithium-iron-phosphate to the delithiated iron-phosphate, the potential curve of LFP is flat. Therefore, it does not contribute any peaks to the IC curves [42,43]. The latter peaks are primarily originating from the different lithiation stages, that the graphite anode undergoes during charging from pure graphite to the fully lithiated stage I (LiC_6), i.e. plateaus represent the following transitions: plateau ① graphite → stage 4 (LiC_{72}), plateau ② stage 3 (LiC_{36}) → stage 2 L (LiC_{12}) and plateau ③ stage 2 (LiC_{12}) → stage 1 (LiC_6) [42,44,45]. Besides the position of the peaks, the width may yield qualitative statements about cell homogeneity [25].

The increased internal resistance is nicely represented by the clearly distinguishable shift of the plateaus ①, ② and ③ towards higher potentials. Observed voltage differences: $\Delta U_{①} = 21.3(8)$ mV, $\Delta U_{②} = 31.1(2)$ mV and $\Delta U_{③} = 27.7(3)$ mV corresponds to an effective difference in the internal resistance $\Delta R = 67.1(9)$ mΩ, which is in good agreement with the estimated DC-resistances. Systematically broader peaks observed for cell 2 correspond to a wider coexistence of multiple lithiation states in the graphite anode, i.e. the lithium distribution in cell 2 is assumed to be more heterogeneous than in cell 1.

Besides this, according to Ref. [42], the relative "height" of ② + ③ peaks reflects the active lithium inventory. Thus, nearly equally "intense" ② + ③ peaks in cell 2 correspond to an almost full lithiation of the graphite anode (attributed to domination of stage 1) in cell 2. For cell 1, a particular discrepancy in the "intensity" of peaks ② + ③ is observed, where higher intensity of signal ② indicated a lower degree of lithium intercalation in its graphite anode. Observed discrepancies can be associated either with initially lower anode lithium inventory or an electrode balancing towards higher anode excess, which cannot be accurately distinguished using $\Delta SoC/\Delta V$ analysis.

Alternatively, the charge profile can be derived as $\Delta V/\Delta SoC$ vs. SoC and the corresponding curves are shown in Fig. 1c. Again, one can resolve processes corresponding to plateaus ①, ② and ③. The phase transition ③ can be unambiguously attributed to stage 2 (LiC_{12}) → stage 1 (LiC_6) transition, which in a perfectly balanced cell should occur at SoC = 0.5. Therefore, it is assumed that the balancing of cell 1 and cell 2 is made with a specific excess of the graphite material, which is systematically higher in cell 1 than in cell 2.

[2] Cell capacity $Q = 1100$ mAh for 18650 type LFP|C cell was reported [9], which yields $\frac{25^2-5^2}{17^2-5^2} \cdot Q = 2497$ mAh for 26650 type cell.

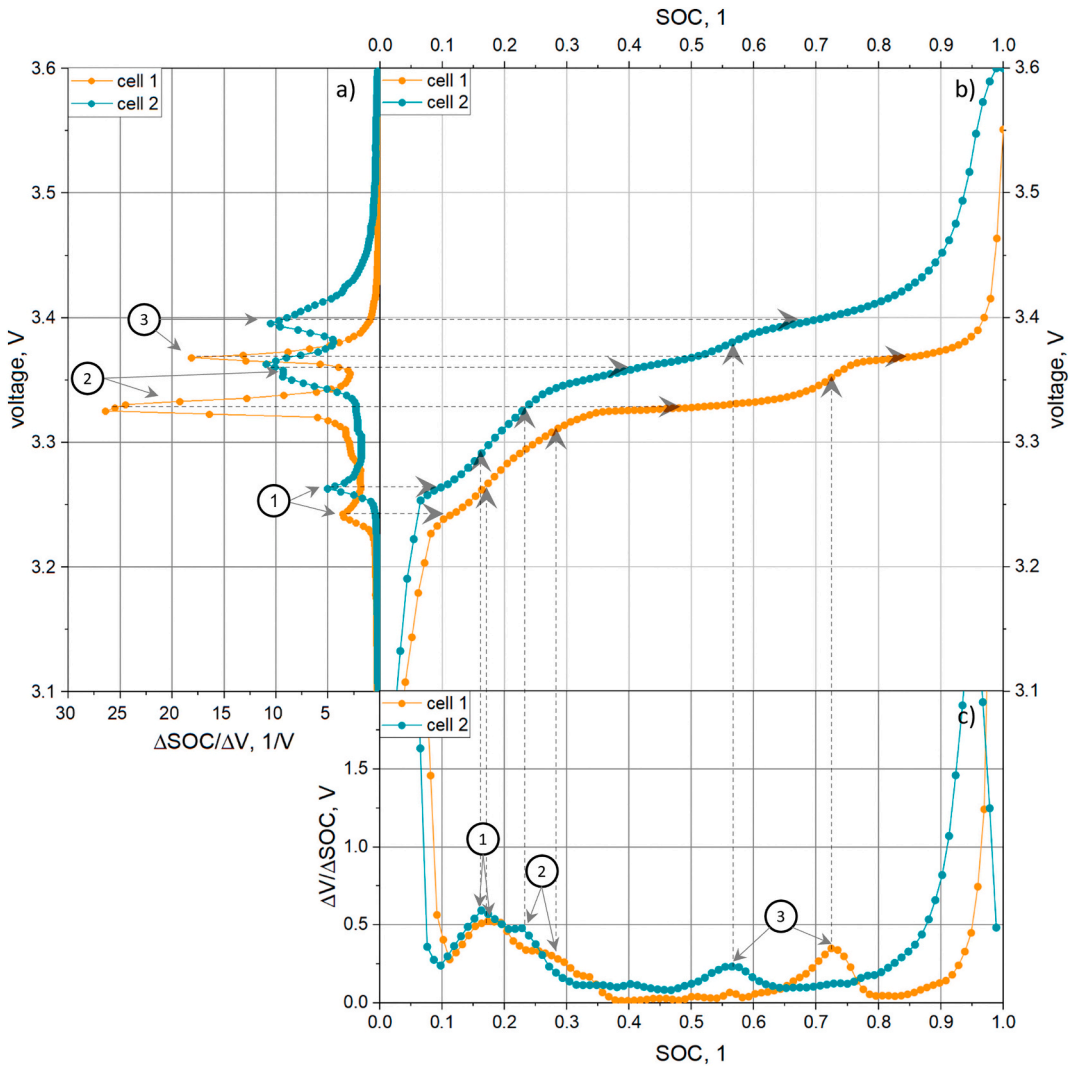

Fig. 1. Incremental capacity analysis a), charge profile upon charging b), and differential voltage analysis c) for two different LFP|C cells of 26650 type. Phase transitions were labeled according to the scheme proposed in Ref. [42], where label ① indicates the coexistence of graphite and LiC_{72} (stage 4); label ② - the transition of stage 3 (LiC_{36}) to stage 2 L (LiC_{12}), label ③ - phase transition between stage 2 (LiC_{12}) and stage 1 (LiC_6).

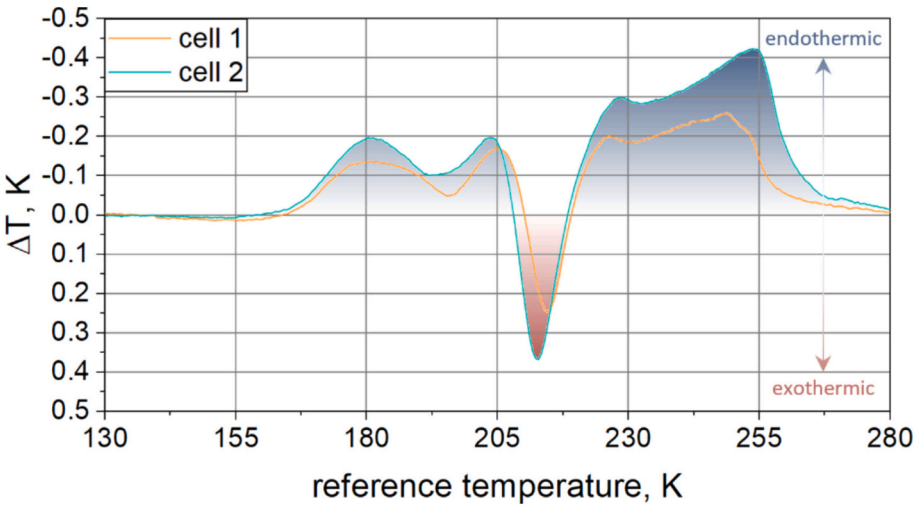

Fig. 2. Shape of differential thermal analysis signal collected for cell 1 and cell 2. Vertical rows and blue-red color gradients indicate the endothermic and exothermic character of the signal. (For interpretation of the references to color in this figure legend, the reader is referred to the web version of this article.)

3.1.2. Differential thermal analysis (DTA)

A lower available lithium inventory in the cell may influence the electrolyte composition [12], resulting in changes in the differential thermal signal. Acquired DTA-curves for both cells are shown in Fig. 2, which qualitatively yield similar signals differing slightly in strength and temperature dependence. Likely, a complex mixture of solvents is utilized, as a series of three endothermic and one exothermic DTA signals were observed in the region of 200–260 K. Such observed thermal signal has been found similar to previously reported M1A 18650-type cell adopting LFP|C chemistry of the same manufacturer (please refer to suppl. Information section in ref. [13]), which permits to assume a similar (but undoubtedly non-identical) electrolyte composition in these cells, also slightly differing in the filling amount. The composition of the electrolyte in cell 1 was determined in ref. [46] as a mixture of conducting salt $LiPF_6$, ethylene carbonate, propylene carbonate, dimethyl carbonate, and ethyl methyl carbonate in a ratio of 30:10:30:30. Based on this, lower available lithium inventory in cell 1 can be attributed to a higher graphite excess.

3.1.3. X-Ray computed tomography

The cell layout, i.e., electrode thickness, current tab distribution, and length, was probed non-destructively using laboratory X-ray computed tomography. Both cells apply a multi-tab approach, using 4 tabs on each electrode. Besides this, cell 1 and cell 2 display specific differences in their design. For example, cell 1 (Fig. 3a) is built using short current tabs of ca. 6.1 mm length (9.3 % of tot. height) connected at the bottom (anode, blue) and ca. 6.3 mm (9.7 % of tot. height) at the top (cathode, red). The four current tabs in cell 1, either at the anode or cathode side, are positioned so that they form a nearly straight line from the center to the cell housing. The anode current tabs are located at 11.5 %, 35.8 %, 61.3 % and 85.5 % relative length of the electrode stripe and the cathode current tabs at 12.0 %, 37.0 %, 64.3 % and 88.2 % relative length, thus being closest to “scheme 4” of electrode connection [11] supplying high power density. This is supported by the relatively thin electrode stack thickness of 276.8 μm. In general, numerous similarities in terms of current tab length, current tab position, electrode thickness between cell 1 and the 18650-type cell [9] from A123 systems were observed. In cell 2 (Fig. 3b), the four current tabs of the anode and the cathode are located at (anode: 17.8 %, 36.7 %, 62.0 %, and 80.3 %; cathode: 12.1 %, 36.9 %, 62.4 %, and 78.9 %) relative length of the electrode stripes without an apparent geometry with respect to their radial or angular position. Each tab extends over the entire height of the electrodes. Such cell design is somewhat unique, i.e., no comparable current tab distribution and length can be found among a series of 18650-type batteries [11]. Again, the four current tabs at each electrode and the thickness of the full electrode stack of 276.4 μm unambiguously point out its potential for high-power application, likewise cell 1.

Both cells inhibit a total number of 39 windings of the electrode stack around the cell center, which was determined along with the thickness of the electrode stack by the distance of the copper current collectors, which are visible in the insets of Fig. 3. Unfortunately, the resolution was not high enough to resolve each individual electrode material.

Virtual vertical cuts through the center of the cell (shown in Fig. S2) identify the electrolyte level in cell 1, whereas no such feature is seen in cell 2. This would further support the assumption of higher electrolyte excess in cell 2, as the whole center pin is filled with electrolyte and not partially as in cell 1 and therefore display no contrast change at the center pin.

3.2. Lithium distribution in fully lithiated graphite anode

The lithium distribution in commercial 18650-type lithium batteries is dependent on the current tab configuration [11], where systematically less lithiation is observed at the location of current tabs and the beginning/end of the anode stripe. Similar to these observations from Ref. [11], distinct lithium distributions can be projected for cells 1 and 2 based on the observed design of the current tabs. The uniformity of the lithium distribution inside the electrodes was probed using a series of diffraction-based spatially resolved characterization tools.

3.2.1. X-ray diffraction computed tomography (XRD-CT)

The local lithium content in the positive and negative electrodes of the studied cells (x in Li_xC_6 and y in Li_yFePO_4) was probed non-destructively using XRD-CT. Studies were carried out on fresh cells in fully charged state, and the in-plane lithium distribution was probed at mid-height. The obtained lithium concentrations are shown in false colors in Fig. 4a for the anodes and Fig. 4b for the cathodes with corresponding distribution histograms in Fig. S3.

A similar lithiation degree of the anode is observed: the plane-averaged lithium content in the graphite anode x in Li_xC_6 for both cells was determined to be $x = 0.91(5)$ and $x = 0.91(8)$ in cell 1 and cell 2, respectively. However, different lithium distribution degrees were stated for cells 1 and 2. Thus, in cell 1, the in-plane Li distribution in the lithium content along the graphite anode stripe was relatively uniform, comparable to cell #34 from Ref. [11]. Cell 2 clearly shows residues of current tabs on its lithium distribution profile, displaying remarkable deviations from the mean values at the current tab locations. Ring-like features with systematically lower lithiation were observed at the position of the current tabs, towards the center pin and cell housing (similar to findings in Ref. [11]). Indications of heterogeneous lithium distribution are also present in the distribution histograms of both cells (Fig. S3). Where a sharp peak is observed in the data of cell 1 (corresponding to a uniform lithium distribution), whilst for cell 2 such peak is sufficiently smeared out, pointing on a more heterogeneous lithiation of the anode.

The averaged in-plane lithium content y in Li_yFePO_4 cathode has been determined as $y = 0.09(8)$ and $y = 0.03(9)$ for fully-charged cell 1 and cell 2, accordingly. Observed lithium distributions in anode and cathode are complementary, i.e., at areas with lower lithium concentrations in the anode, the lithium content in the cathode is higher and vice versa. In contrast to the anode, in cell 1, the lithiation of the cathode displays a weak gradient along the electrode stripe from the cell center towards the cell housing, showing systematically higher lithium concentrations at the electrode part closer to the outer edge. For cell 2, the location of the current tabs at the anode (displaying the systematically lower state of lithiation) is characterized by the higher lithium contents at the cathode side. Comparing the lithium distribution of cell 1 to 18650-type LFP|C cell #34 in Ref. [11], one can state that the multi-tab approach in cell 1 was successful in smoothing out the edge inhomogeneities present in the single-table 18650-type LFP|C battery [9].

Based on the observed differences between x and y in cells 1 and 2, one can introduce an “exchange” or “activity” map A defined as $A = x\text{-}y$ reflecting the local “usage” of the electrode materials, i.e. the degree to which its potential capacity is utilized. Mean in-plane electrode “usage” is determined for cells 1 and 2 as $A = 0.83(8)$ and $A = 0.88(2)$, showing that cell 2 is potentially more “stressed” during cycling (when compared to cell 1). In such a way, quantified electrode stress degrees may directly impact the cell life. To assess the spatial information, the deviation of A from its median is presented in Fig. 4c for both cells. Plotted distributions reveal the “exchange” parameter A homogeneously distributed over the mid-plane of cell 1, while cell 2 displays more substantial deviations with systematically lower activities occurring at every current tab location. Positions with higher activities A display the highest accommodated stress during cell cycling, leading to faster material degradation and, correspondingly, shorter lifetimes. Based on the above-mentioned, it can be stated that despite the initially higher cell 2 capacity, the extended local cell “usage” would lead to faster degradation of cell 2 compared to cell 1.

The obtained resolution of $1 \times 1\ mm^2$ of the XRD-CT measurement is obviously insufficient to resolve individual layers of the electrode jelly roll. Therefore, a tracking of detailed lithium distribution of the individual electrode layers with high spatial resoltuon as reported in

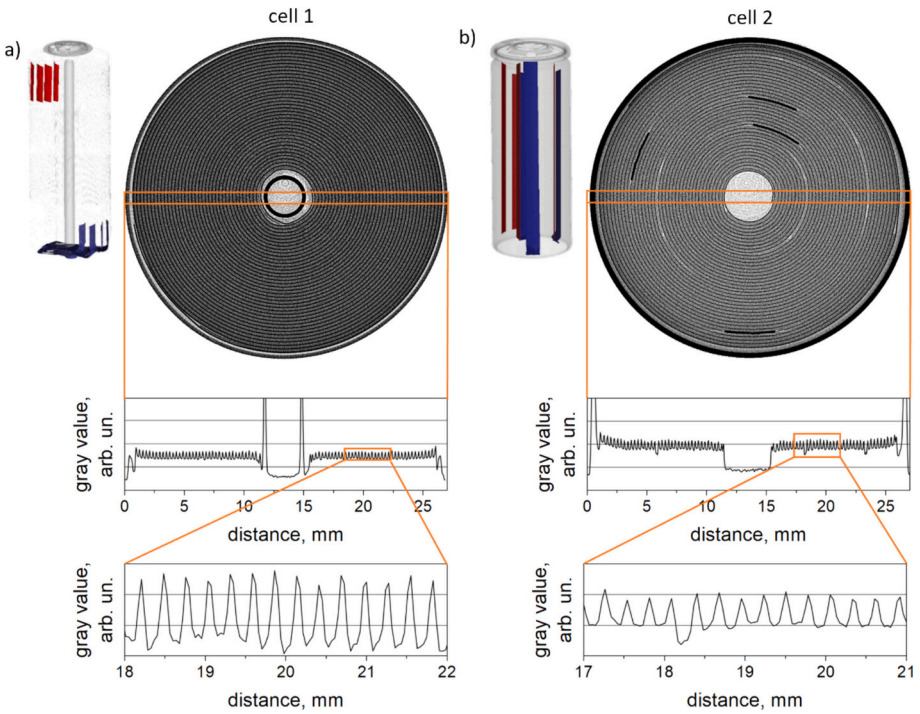

Fig. 3. Non-destructive X-ray CT characterization: 3D reconstruction of layouts for cell 1 (a) and cell 2 (b). Current tabs at positive and negative electrodes/current collectors are presented in blue and red, respectively. The radial line profile is obtained from a slice through the cell at middle height. This 1D profile reveals a gray scale pattern, indicating the electrode stack thickness. (For interpretation of the references to color in this figure legend, the reader is referred to the web version of this article.)

previous literature [9,14,15,17] was not possible. Microscopic effects like the influence of electrode delamination, particle cracking etc. are not visible with such low resolution. Nevertheless, the resolution is sufficient to resolve gradients occurring at a macroscopic length scale of the cell dimension, i.e. cell aging mechanisms like reduction of intercalated lithium. To investigate challenges on a microscopic scale, smaller beam sizes are required, which leads to a larger number of translation/rotation scans, causing an enormous increase in beamtime. Besides the reduction in exposure time, capable of compensating for a large number of translation/rotation scans by using brilliant synchrotron sources, one could region of interest diffraction computed tomography measurements, which could potentially achieve high (sub μm) spatial resolution on a field of view covering a thickness of electrode (e.g., 100 μm).

To check for the influence of the short current tab length for cell 1, the XRD-CT data were collected at two more planes (above and below the middle). Corresponding lithium distributions for x and y in Li_xC_6 and Li_yFePO_4 and the "activity" distribution are shown in Fig. S4, along with their plane-averaged profile over the height of cell 1 in Fig. S5. Lithium distribution in the LFP cathode has been found quasi-independent of the cell height, whilst the anode displays pronounced height dependence, showing generally lower lithiation at the cell top and bottom and the amount of intercalated lithium systematically higher at the current tab location. Comparing the lithium distributions at different heights confirms the height gradient of lithium distribution. The observed peculiarities can be directly attributed to lower electrode usage at the cell top, potentially enhancing lifetime and faster lithium exchange in cell 1. However, due to beam time limitations, no detailed height scans could be performed, and this needs to be addressed in the future.

3.2.2. *Spatially-resolved neutron powder diffraction*

Coherent elastic neutron scattering was used as a probe to gather information about the lithium content in the graphite anode in the center of cell 1. Due to nuclear interaction character, the penetration depth of thermal neutrons is higher than that of high-energy X-ray photons interacting with the electron shells of the atoms. The lithium distribution x in the lithiated graphite anode Li_xC_6 in the mid-plane of a fully charged 26650-type battery was derived from a spatially resolved neutron diffraction dataset and is shown in Fig. 5 along with the corresponding distribution histogram as inset. The average lithium content $\overline{x}$ in Li_xC_6 is determined to be $\overline{x}$=0.88(6), which agrees with the average value from the XRD-CT experiment. The experimental findings from the XRD-CT experiment with a plateau-like lithium distribution and no influence from the current tabs can be confirmed. Furthermore, the plateau-like behavior is even more pronounced towards the cell center, with a steep decrease near the center pin. The homogeneous lithium distribution can be identified best in the distribution histogram (inset in Fig. 5). A sharp peak in the histogram with a center at x = 0.95(2) corresponds to the plateau (as proposed in Ref. [11]) along with a small tail towards lower values originating from the outer and inner cell regions, confirming the homogeneous lithium distribution in cell 1.

Besides the in-plane characterization, a "gauge" volume scan at various heights was performed. The obtained height-dependent lithium content within the chosen gauge volume is displayed in Fig. S5 and shows a pronounced height distribution of lithiation (similar to that reported in Ref. [33]). This could either be attributed to the current distribution across the "width" of the electrode stripe or a missing electrode coating due to the current tabs at top and bottom.

3.3. *Cell aging*

To characterize how these differences (cell geometry, electrolyte filling, lithium heterogeneity) affect the aging behavior, the cells were cycled as described in Section 2.6. DTA and X-ray CT measurements were repeated afterwards. By comparing the cell capacity over the number of cycles in Fig. S7, one can see that cell 2 displayed a significantly shorter cycling lifetime (end at approx. 600 cycles) compared to cell 1. Fast degradation already takes place during the first 125 cycles, where a fast capacity loss between cycles 30 and 70 can be seen with a subsequent change of slope between cycles 70 and 125, which results in

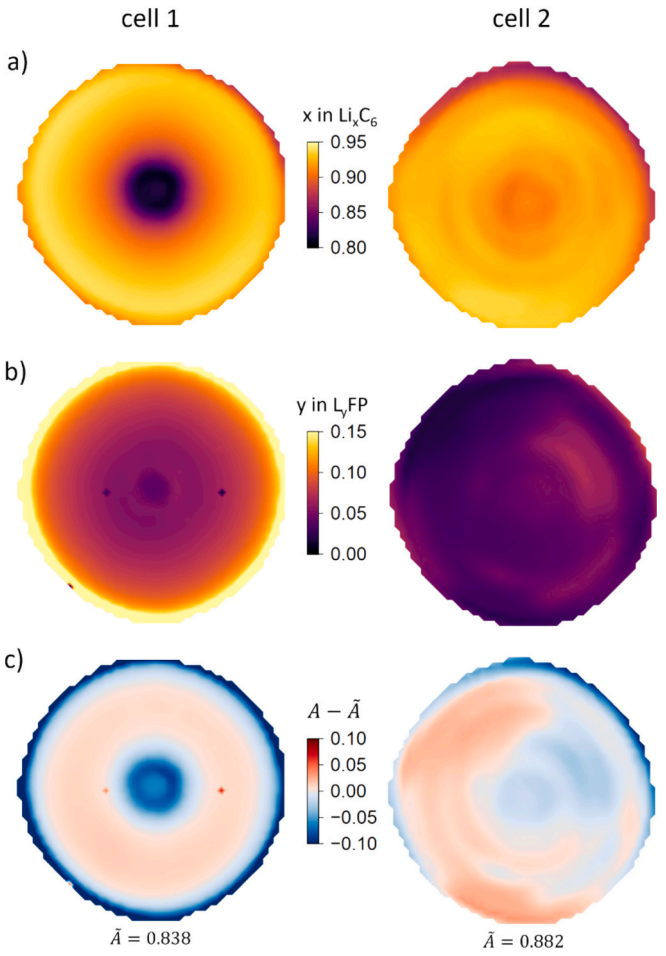

Fig. 4. In-plane lithiation states of battery electrodes in 26650-type cells - x in Li_xC_6 in the graphite anode (top) and y in Li_yFePO_4 cathode (middle) for cell 1 (left) and cell 2 (right). In-planed distribution of electrode "usage" $A - \tilde{A}$ (bottom).

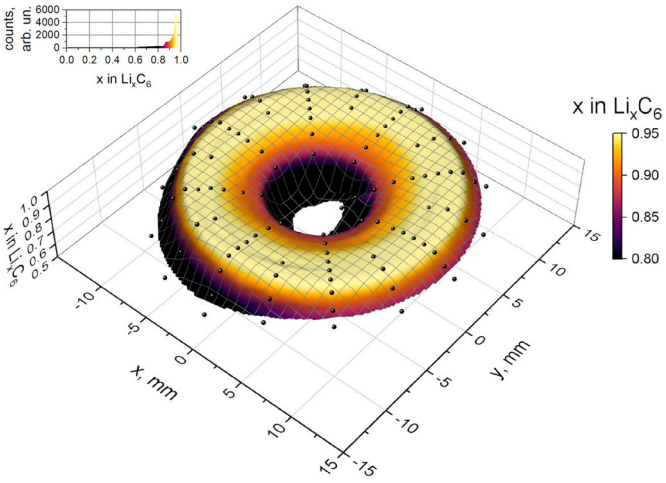

Fig. 5. In-plane (at middle cell height) distribution of x in lithiated graphite anode Li_xC_6 of cell 1 in fully charged state as determined by spatially-resolved neutron powder diffraction. The inset corresponds to the histogram of the lithium distribution.

a total capacity increase of 24.7 mAh between cycles 70 and 125. After this slight increase, the capacity drops rapidly to 908.5 mAh (i.e. 40 % of initial capacity) after only 611 cycles. Cell 1, however, shows an expected regular three-step capacity decrease as described in literature before [38,47,48].

The observed capacity fading is complemented by charge profile changes, reflected in the deviations between state-of-health dependent ICA and DVA indicators (shown in Fig. S8 for cell 1 and Fig. S9 for cell 2, as determined for the check-up cycles). The voltage profile obtained during the cycling of the cells represents only the average behavior of the complete electrode material. As there is a wide variety of aging mechanisms with complex interplay [47,49], individual and local degradation cannot be determined with DVA and ICA. Nevertheless, a more general statement regarding the aging of the cells can be made. Standard features can be identified in the fading behavior of cell 1 and cell 2: first, the peaks in the DVA data shift to higher values, resulting from an increasing internal cell resistance; second, the intensity of the second and especially the third peak is decreasing with increasing cycle number. This corresponds to a lower lithiation degree, i.e., LiC_{12} and LiC_6 formed during charging, and accordingly reflects the loss of active/movable lithium in the cells. In cell 1, the peak width remains almost unchanged, unlike cell 2, where the peaks display a distinct systematic broadening. This observation can be attributed to a more homogeneous lithiation of cell 1 (with a precise sequence in the phase formation during graphite lithiation), while in cell 2, a coexistence of many different lithiated graphites is expected at any given SOC. These conclusions are supported by the ICA data, in which characteristic peaks are shifted towards higher SOCs. This indicates that the formation of the lithiated graphites starts at higher SOC and, therefore, leads to the formation of a smaller amount of higher lithiated phases overall.

DTA measurements were repeated after the cell cycling, where the remaining capacity for both cells was at about the same level (Fig. S10). The DTA data of the aged cells display similarities (as in the fresh state), potentially indicating a similar character of electrolyte aging/degradation (SEI formation, function of additives, etc.). In the aged state the observed signal from cell 2 is again higher than the one from cell 1, attributed to a higher amount of electrolyte. Before and after the cycling, the electrolyte level remained the same in cell 1, as revealed by vertical cuts through the reconstructed cell volume (Fig. S2). Based on this, the observed changes (and similar to the observations in Ref. [13]) in the DTA signal can be assigned to the consumption of additives, conducting salt, etc., and not of the organic solvents themselves.

During the dis-/charging of a LIB, lithium-ions are exchanged between the cathode and anode, supplying a mass/ionic transport between the electrodes and leading to modifications in the crystal structure (primarily the lattice dimensions) of the electrode materials. Structural changes on the nanometer level lead to macroscopic changes in LIB dimensions, i.e., „cell breathing", which reflects the cell SOC. Extensive cell cycling induces dynamic changes of LIB dimensions, which can be divided into reversible (SOC-dependent) and irreversible (typically SOH-dependent) parts. Irreversible changes in the cell/electrode arrangement are becoming increasingly important as they affect the performance and safety of LIBs. X-ray CT unambiguously revealed changes in the cell interior after the electrochemical cycling. Reconstructed images at the top, middle, and bottom of the aged cells are shown[3] in Fig. S11. In cell 1 (when comparing fresh and aged states), three kinds of geometrical degradations can be stated:

- the initial empty gap between the electrode jellyroll and the center pin decreased; as well as the gap towards the cell housing

[3] Note: a common cell 1 was used in all measurements, whilst cell 2 was represented by several cells from the same batch - used in the other measurements.

- certain deformations and delamination of the electrode stack took place at the position of the inner anode current tab along the entire cell height;
- a small ring of delaminated electrodes occurred at the position of the negative current tabs towards the cell housing.

In agreement with the location where the ring of delaminated electrode material is observed, the radius of the cell housing has increased. This means that the cell housing has undergone an inelastic deformation. This effect was further probed using optical micrometry on fresh and aged cells. Deviations of the cell radius are presented in false color for different cell orientations in Fig. S12. Here, the localized ring of increased cell radius (ca. 100 μm) can be identified. The thickness of the cell mandrel was determined to be 322 ± 8 μm made out of a different material from the top and bottom parts, which may also influence the expansion behavior of this cell. and 334.5 ± 19.5 μm.

When compared to cell 1, the mechanical degradation of cell 2 was found to be more pronounced: the gap between cell housing and electrode spiral increased, accompanied by a substantial reduction of the empty space in the center of the cell. The deformation of the jellyroll is substantial and most significant at the inner anode current tab, but the missing center pin facilitates cell deformation throughout the complete cell radius and height, leading to bent and displaced current tabs. Furthermore, the current tabs at both the anode and cathode change their positions in the cell, indicating a twist/shift of the electrode stripes with respect to each other. Therefore, the observed deviations cannot solely be attributed to the tab structure but could result from slight deviations in the manufacturing process. In this case, the observed substantial mechanical deformation of the cell jellyroll could be a reason for the accelerated capacity degradation of cell 2. It is worth noting that despite the considerable deformation of the electrodes towards the cell center, the cell housing underwent nearly no deformation with increasing cycle number (Fig. S13). The thickness of the mandrel was determined to be 334.5 ± 19.5 μm of steel, which is slightly thicker than in cell 1. The finding of optical micrometry highlights the extreme relevance of depth-resolved studies of LIBs.

4. Summary/conclusion

Two LFP|C high-power batteries of 26650-type were studied non-destructively using various experimental characterization tools to probe the uniformity of the battery components. Despite similar cell chemistry and form factor, several differences were noticed, reflected in the electrochemical behavior, cell layout, and lithium distribution. Differences in charging profiles were observed and attributed to differences in cell balancing and the available mobile lithium. A similar electrolyte mixture for both cells was concluded based on DTA measurements. A non-destructive look into the interior of studied 26650-type cells revealed essentially different layouts of the electrical connection of the electrodes in the studied cells. A multi-tab approach was realized in both cells with 8 current tabs per cell, four connecting the positive and four connecting the negative electrode stripes. However, two different connection schemes were applied, as revealed by X-ray CT, which seems to affect the lithium distribution in the cells. Potentially advantageous current tab-free configuration was evaluated and discussed, where an assumption about more uniform cell usage as a source of increasing the cell lifetime has been made.

The cell aging of both cells has been investigated and discussed using the above-mentioned techniques. Two significantly different cell lifetimes have been observed, along with substantial mechanical deformation of the electrodes in the short-life cell observed with X-ray CT. On the other hand, the first cell showed a slight deformation of the cell housing in the region where the negative current tabs are located. Additionally, electrochemical cycling data analysis hints at a more heterogeneous lithium distribution in the short-life cell. Changes in the DTA signal were similar in both cells after aging, corresponding to a similar aging behavior of the electrolyte components.

Cell-to-cell variations being present in the manufacturing of commercial lithium-ion batteries is subject to current research and will undoubtedly influence the results of studies utilizing a limited number of samples [50,51]. In this study, the number of single measurements was bound to limited beamtime at large-scale research facilities (synchrotron and/or neutron). Nevertheless, current results fit the overall picture of expected lithium distribution, cell aging mechanisms etc. Another task that has to be tackled in future works (but is considered to be out of scope in the current manuscript) is the influence of different cell cycling procedures stabilizing different cell aging [52]. To simulate the most realistic aging behavior of batteries used in electric vehicles, automotive-like conditions applying, e.g., WLTP/EPA protocols, would provide more accurate results [53].

In summary, the inner structure of 26650-type Li-ion batteries was successfully studied non-destructively, opening promising opportunities for the characterization of larger-format cylinder-type batteries of 4680 or 4890 types, which are actively developed at the moment. The current manuscript's main unexpected finding was that the shape of the cell housing does not reflect the deformation of the cell interior, indicating the complex mechanical behavior of the jellyroll, creating the case for the urgent need for spatially resolved, non-destructive characterizations of the large format LIBs.

CRediT authorship contribution statement

D. Petz: Writing – original draft, Visualization, Validation, Software, Formal analysis. **M.J. Mühlbauer:** Writing – review & editing, Validation, Methodology, Investigation, Formal analysis. **V. Baran:** Writing – review & editing, Validation, Resources, Investigation, Formal analysis, Data curation. **J. Rebelo Kornmeier:** Writing – review & editing, Visualization. **A. Schökel:** Writing – review & editing, Resources, Project administration, Data curation. **T. Pirling:** Writing – review & editing, Resources, Data curation. **P. Müller-Buschbaum:** Writing – review & editing, Supervision, Project administration, Funding acquisition. **A. Senyshyn:** Writing – original draft, Validation, Software, Project administration, Methodology, Investigation, Funding acquisition, Formal analysis, Data curation, Conceptualization.

Declaration of competing interest

The authors declare that they have no known competing financial interests or personal relationships that could have an influence on the work reported in this paper.

Acknowledgments

The authors gratefully acknowledge the financial support provided by the Heinz Maier-Leibnitz Zentrum (Technische Universität München), German Federal Ministry of Education and Research (BMBF project 05K16VK2). Authors thank the Heinz Maier-Leibnitz Zentrum and Institute Laue - Langevin for providing beamtime and access to their infrastructure. The authors acknowledge DESY (Hamburg, Germany), a member of the Helmholtz Association HGF, for providing experimental facilities. Parts of this research were carried out at PETRA III using beamline P02.1. Beamtime was allocated for beamtime C-20010001.

Appendix A. Supplementary data

Supplementary data to this article can be found online at https://doi.org/10.1016/j.est.2025.115911.

Data availability

Data will be provided by the authors upon reasonable request.

References

[1] W. Huang, et al., Questions and answers relating to lithium-ion battery safety issues, Cell Reports Physical Science 2 (1) (2021) 100285.
[2] C. Shi, et al., Accordion-like stretchable Li-ion batteries with high energy density, Energy Storage Materials 17 (2019) 136–142.
[3] X. Wang, et al., Rechargeable solid-state lithium metal batteries with vertically aligned ceramic nanoparticle/polymer composite electrolyte, Nano Energy 60 (2019) 205–212.
[4] S.V. Erhard, et al., Simulation and measurement of the current density distribution in lithium-ion batteries by a multi-tab cell approach, J. Electrochem. Soc. 164 (1) (2017) A6324.
[5] G. Zhang, et al., Effects of non-uniform current distribution on energy density of Li-ion cells, J. Electrochem. Soc. 160 (11) (2013) A2299.
[6] G. Zhang, et al., In-situ measurement of current distribution in a Li-ion cell, J. Electrochem. Soc. 160 (4) (2013) A610.
[7] G. Zhang, et al., In situ measurement of radial temperature distributions in cylindrical Li-ion cells, J. Electrochem. Soc. 161 (10) (2014) A1499.
[8] J.B. Robinson, et al., Non-uniform temperature distribution in Li-ion batteries during discharge – a combined thermal imaging, X-ray micro-tomography and electrochemical impedance approach, J. Power Sources 252 (2014) 51–57.
[9] D. Petz, et al., Lithium distribution and transfer in high-power 18650-type Li-ion cells at multiple length scales, Energy Storage Materials 41 (2021) 546–553.
[10] D.P. Finegan, et al., Spatial dynamics of lithiation and lithium plating during high-rate operation of graphite electrodes, Energy Environ. Sci. 13 (8) (2020) 2570–2584.
[11] D. Petz, et al., Heterogeneity of graphite lithiation in state-of-the-art cylinder-type Li-ion cells, Batteries Supercaps 4 (2) (2021) 327–335.
[12] D. Petz, et al., Lithium heterogeneities in cylinder-type Li-ion batteries – fatigue induced by cycling, J. Power Sources 448 (2020) 227466.
[13] D. Petz, et al., Aging-driven composition and distribution changes of electrolyte and graphite anode in 18650-type Li-ion batteries, Adv. Energy Mater. n/a(n/a) (2022) 2201652.
[14] A. Vamvakeros, et al., Cycling rate-induced spatially-resolved heterogeneities in commercial cylindrical Li-ion batteries, Small Methods 5 (9) (2021) 2100512.
[15] D. Matras, et al., Emerging chemical heterogeneities in a commercial 18650 NCA Li-ion battery during early cycling revealed by synchrotron X-ray diffraction tomography, J. Power Sources 539 (2022) 231589.
[16] T.M.M. Heenan, et al., Mapping internal temperatures during high-rate battery applications, Nature 617 (7961) (2023) 507–512.
[17] E. Lübke, et al., The origins of critical deformations in cylindrical silicon based Li-ion batteries, Energy Environ. Sci. 17 (14) (2024) 5048–5059.
[18] D. Petz, et al., Heterogeneity of lithium distribution in the graphite anode of 21700-type cylindrical Li-ion cells during degradation, Batteries 10 (3) (2024) 68.
[19] W. Zhao, G. Luo, C.-Y. Wang, Effect of tab design on large-format Li-ion cell performance, J. Power Sources 257 (2014) 70–79.
[20] K.-J. Lee, et al., Three dimensional thermal-, electrical-, and electrochemical-coupled model for cylindrical wound large format lithium-ion batteries, J. Power Sources 241 (2013) 20–32.
[21] M.S.D. Darma, et al., Managing life span of high-energy LiNi0.88Co0.11Al0.01O2|C–Si Li-ion batteries, ACS Applied Energy Materials 4 (9) (2021) 9982–10002.
[22] J. Zhu, et al., Investigation of lithium-ion battery degradation mechanisms by combining differential voltage analysis and alternating current impedance, J. Power Sources 448 (2020) 227575.
[23] P. Keil, et al., Calendar aging of lithium-ion batteries, J. Electrochem. Soc. 163 (9) (2016) A1872.
[24] K. Ando, T. Matsuda, D. Imamura, Degradation diagnosis of lithium-ion batteries with a LiNi0.5Co0.2Mn0.3O2 and LiMn2O4 blended cathode using dV/dQ curve analysis, J. Power Sources 390 (2018) 278–285.
[25] H. Kato, Y. Kobayashi, H. Miyashiro, Differential voltage curve analysis of a lithium-ion battery during discharge, J. Power Sources 398 (2018) 49–54.
[26] M. Lewerenz, et al., Differential voltage analysis as a tool for analyzing inhomogeneous aging: a case study for LiFePO4|graphite cylindrical cells, J. Power Sources 368 (2017) 57–67.
[27] M.K.G. Bauer, et al., Lithium-ion differential thermal analysis studies of the effects of long-term Li-ion cell storage on electrolyte composition and implications for cell state of health, J. Electrochem. Soc. 170 (3) (2023) 030543.
[28] R.P. Day, et al., Differential thermal analysis of Li-ion cells as an effective probe of liquid electrolyte evolution during aging, J. Electrochem. Soc. 162 (14) (2015) A2577.
[29] M.K.G. Bauer, J.R. Dahn, Using lithium-ion differential thermal analysis to probe tortuosity of negative electrodes in lithium-ion cells, J. Electrochem. Soc. 168 (2) (2021) 020501.
[30] C.A. Schneider, W.S. Rasband, K.W. Eliceiri, NIH image to ImageJ: 25 years of image analysis, Nat. Methods 9 (7) (2012) 671–675.
[31] U. Ayachit, The ParaView Guide: A Parallel Visualization Application, Kitware, Inc., 2015.
[32] T. Pirling, G. Bruno, P.J. Withers, SALSA—a new instrument for strain imaging in engineering materials and components, Mater. Sci. Eng. A 437 (1) (2006) 139–144.
[33] A. Senyshyn, et al., Homogeneity of lithium distribution in cylinder-type Li-ion batteries, Sci. Rep. 5 (1) (2015) 18380.
[34] A.-C. Dippel, et al., Beamline P02.1 at PETRA III for high-resolution and high-energy powder diffraction, J. Synchrotron Radiat. 22 (3) (2015) 675–687.
[35] A. Vamvakeros, et al., Interlaced X-ray diffraction computed tomography, J. Appl. Crystallogr. 49 (2) (2016) 485–496.
[36] J. Kieffer, et al., New tools for calibrating diffraction setups, J. Synchrotron Radiat. 27 (2) (2020) 558–566.
[37] D. Gürsoy, et al., TomoPy: a framework for the analysis of synchrotron tomographic data, J. Synchrotron Radiat. 21 (Pt 5) (2014) 1188–1193.
[38] X. Lin, et al., A comprehensive capacity fade model and analysis for Li-ion batteries, J. Electrochem. Soc. 160 (10) (2013) A1701.
[39] Networked Instrument COntrol System (NICOS), Available from: https://www.nicos-controls.org/, 23.07.2024.
[40] J. Ahrens, B. Geveci, C. Law, 36 - ParaView: an end-user tool for large-data visualization, in: C.D. Hansen, C.R. Johnson (Eds.), Visualization Handbook, Butterworth-Heinemann, Burlington, 2005, pp. 717–731.
[41] J. Schindelin, et al., Fiji: an open-source platform for biological-image analysis, Nat. Methods 9 (7) (2012) 676–682.
[42] A. Krupp, et al., Incremental capacity analysis as a state of health estimation method for lithium-ion battery modules with series-connected cells, Batteries 7 (1) (2021) 2.
[43] P. Hou, et al., Li-ion batteries: phase transition, Chin. Phys. B 25 (1) (2016) 016104.
[44] T. Ohzuku, Y. Iwakoshi, K. Sawai, Formation of lithium-graphite intercalation compounds in nonaqueous electrolytes and their application as a negative electrode for a lithium ion (shuttlecock) cell, J. Electrochem. Soc. 140 (9) (1993) 2490–2498.
[45] J.R. Dahn, Phase diagram of ${\mathrm{Li}}_{\mathit{x}}$${\mathrm{C}}_{6}$, Phys. Rev. B 44 (17) (1991) 9170–9177.
[46] T. Taskovic, et al., An investigation of Li-ion cell degradation caused by simulated autoclave cycles, J. Electrochem. Soc. 171 (6) (2024) 060520.
[47] J.S. Edge, et al., Lithium ion battery degradation: what you need to know, Phys. Chem. Chem. Phys. 23 (14) (2021) 8200–8221.
[48] Y. Liao, et al., Electrolyte degradation during aging process of lithium-ion batteries: mechanisms, characterization, and quantitative analysis, Adv. Energy Mater. 14 (18) (2024) 2304295.
[49] C.R. Birkl, et al., Degradation diagnostics for lithium ion cells, J. Power Sources 341 (2017) 373–386.
[50] D. Beck, et al., Inhomogeneities and cell-to-cell variations in lithium-ion batteries, a review, Energies 14 (11) (2021) 3276.
[51] P. Dechent, et al., Estimation of Li-ion degradation test sample sizes required to understand cell-to-cell variability, Batteries & Supercaps 4 (12) (2021) 1821–1829.
[52] P. Keil, A. Jossen, Charging protocols for lithium-ion batteries and their impact on cycle life—an experimental study with different 18650 high-power cells, Journal of Energy Storage 6 (2016) 125–141.
[53] G. Sordi, et al., Degradation of lithium-ion batteries under automotive-like conditions: aging tests, capacity loss and q-OCP interpretation, Future Batteries 3 (2024) 100005.